

The influence of Laser Relative Intensity Noise in the Laser Interferometer Space Antenna (LISA)

L. Wissel,^{1,2} O. Hartwig,³ J.B. Bayle,⁴ M. Staab,^{1,2} E.D. Fitzsimons,⁵ M. Hewitson,^{1,2} and G. Heinzel^{1,2}

¹*Max Planck Institute for Gravitational Physics (Albert-Einstein-Institut), 30167 Hannover, Germany*

²*Leibniz Universität Hannover, 30167 Hannover, Germany*

³*SYRTE, Observatoire de Paris-PSL, CNRS, Sorbonne Université, LNE, Paris, France*

⁴*University of Glasgow, Glasgow G12 8QQ, United Kingdom*

⁵*The UK Astronomy Technology Centre, Royal Observatory, Edinburgh, Blackford Hill, Edinburgh, EH9 3HJ, UK*

(Dated: January 5, 2023)

The Laser Interferometer Space Antenna (LISA) is an upcoming ESA mission that will detect gravitational waves in space by interferometrically measuring the separation between free-falling test masses at picometer precision. To reach the desired performance, LISA will employ the noise reduction technique Time-Delay Interferometry (TDI), in which multiple raw interferometric readouts are time shifted and combined into the final scientific observables. Evaluating the performance in terms of these TDI variables requires careful tracking of how different noise sources propagate through TDI, as noise correlations might affect the performance in unexpected ways. One example of such potentially correlated noise is the Relative Intensity Noise (RIN) of the six lasers aboard the three LISA satellites, which will couple into the interferometric phase measurements. In this article, we calculate the expected RIN levels based on the current mission architecture and the envisaged mitigation strategies. We find that strict requirements on the technical design reduce the effect from approximately $8.7 \text{ pm}/\sqrt{\text{Hz}}$ per inter-Spacecraft (SC) interferometer to that of a much lower sub- $1 \text{ pm}/\sqrt{\text{Hz}}$ noise, with typical characteristics of an uncorrelated readout noise after TDI. Our investigations underline the importance of sufficient balanced detection of the interferometric measurements.

PACS numbers: 07.05.Kf, 07.50.Qx, 07.60.Ly, 07.87.+v, 42.62.Eh, 95.55.Ym

I. INTRODUCTION

The Laser Interferometer Space Antenna (LISA) is a future space mission that will detect gravitational waves in the mHz range [1, 2]. It consists of a constellation of three identical Spacecraft (SC), each of which follows a heliocentric orbit at similar distance to the Sun as the Earth, such that the whole constellation forms an almost equilateral triangle either leading or trailing our planet with an angular separation of (10 to 30)°. Each spacecraft hosts two free-falling Test Masses (TMs), which are shielded inside the SCs from external disturbances and act as geodesic reference points for the gravitational wave detection. Laser beams are exchanged between the SCs across the 2.5 Gm arms of the constellation, tracking the distance variations between the TMs. Due to orbital dynamics, the frequencies of the inter-SC lasers will be subject to Doppler shifts in the MHz band, such that the interferometers onboard LISA will detect heterodyne frequencies with a bandwidth of about (5 to 25) MHz. Distance fluctuations between the spacecraft and the TMs housed within them will be encoded as phase fluctuations in these MHz beatnotes, which the LISA phasemeters will be able to resolve with μ -cycle precision, corresponding to a design sensitivity of about $10 \text{ pm}/\sqrt{\text{Hz}}$.

This ultra precise measurement will enable LISA to simultaneously detect and characterize tens of thousands of gravitational-wave sources, potentially answering many open questions in astrophysics, cosmology and fundamental physics.

The precursor mission LISA Pathfinder (LFP) already demonstrated the feasibility of many parts of the system [3, 4], including the local interferometry inside each SC up to approximately $30 \text{ fm}/\sqrt{\text{Hz}}$ precision [5, 6]. The inter-satellite interferometry has been partially demonstrated with the GRACE-FO mission [7].

However, LISA presents a number of unique technical challenges. Contrary to GRACE-FO, the raw readout of the inter-satellite interferometers of LISA will be completely overwhelmed by laser frequency noise, which does not immediately cancel, due to the time-varying and unequal arms of the constellation. Instead, LISA will make use of post processing techniques such as Time-Delay Interferometry (TDI), in which multiple interferometric readouts are combined with the appropriate delays to suppress the dominant noise sources, such as laser frequency noise [8]. These techniques, together with strict requirements that are placed on the subsystems and lasers, will ensure that LISA reaches its sensitivity goal. Different noises propagate through TDI with various transfer functions [9], depending on their characteristics, such that evaluating the final performance of LISA requires detailed studies for all performance relevant noise sources.

One of these noises is laser Relative Intensity Noise (RIN), which is typically described by the laser power fluctuations relative to its average power. Since it is a property of each laser, it propagates through the constellation into the various interferometers and generates additive power noise to the time-varying beat signals on

every Photodiode (PD). This noise couples inevitably to the phase readout at around the heterodyne frequency (so called “1f-RIN”) and its first harmonic (“2f-RIN”) [10]. We show in this article that it is one of the dominating metrology noise sources (after removal of laser frequency noise) if not carefully controlled. 1f-RIN is typically the biggest contributor, since the resulting phase noise is scaled by the ratio of the beam powers, which are, for LISA, fairly large (magnification in the long-arm interferometers by about 7 orders of magnitude). As such, its impact on the sensitivity has to be understood and mitigated.

We draw on the lessons learned from the LPF mission that has also been used to study the effect of RIN in a space-based heterodyne interferometer. In this article we describe the coupling in the context of the LISA mission architecture, taking into account the constellation characteristics, possible correlations, the optical parameters and the effects of LPF-comparable mitigation schemes.

Further, we study the impact of TDI on the RIN phase error by means of simulation and compare it with analytical expectations. We find that the coupling exhibits performance characteristics similar to that of an uncorrelated sub-1 pm/ $\sqrt{\text{Hz}}$ noise, assuming reasonable implementation of the mitigation strategies.

II. MISSION CHARACTERISTICS WITH RESPECT TO RIN

In this section, we give an overview of important mission aspects that have an effect on the RIN-to-phase coupling. The theory of the coupling itself will be discussed in later sections.

In Fig. 1, a schematic of the constellation with the commonly-used nomenclature is shown. The main measurement is the “virtual” TM-to-TM measurement along one LISA arm. For technical reasons (e.g., beam divergence over millions of kilometers, very weak beam powers, straylight effects and optical design), no direct TM-to-TM measurements are possible. Therefore, we use the “split-interferometry” setup, in which 3 optical measurements are combined to reconstruct the desired quantity: the local TM-to-local SC measurement, the local SC-to-distant SC measurement, and the distant SC-to-distant TM measurement.

The total single link TM-to-TM metrology noise is considered to be below $10 \text{ pm}/\sqrt{\text{Hz}}$,

$$S_{\text{IFO}}^{1/2} \leq 10 \frac{\text{pm}}{\sqrt{\text{Hz}}} \cdot \sqrt{f_R}, \quad (1)$$

$$f_R = 1 + \left(\frac{2 \text{ mHz}}{f} \right)^4, \quad (2)$$

with f_R as a factor allowing for a relaxation towards lower frequencies, where acceleration noise becomes dominant and testing is difficult [1].

The lasers have an output power of 2 W at 1064 nm [1],

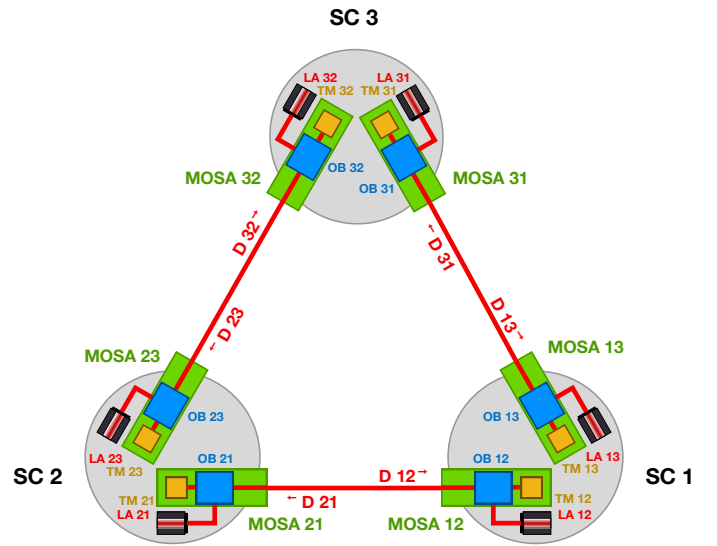


FIG. 1. Simplified overview of the LISA triangular constellation with the naming conventions as used in this article. Delays are denoted D_{ij} ; Optical Benches OB_{ij} ; lasers are called LA_{ij} . Reprint from [11].

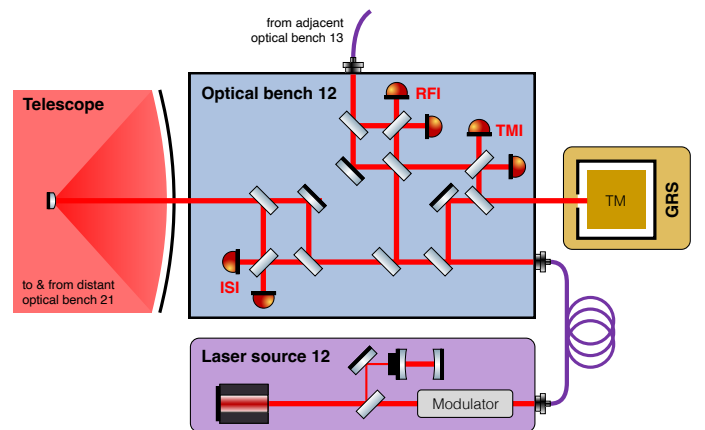


FIG. 2. Schematic of the optical interferometry on one LISA MOSA from Fig. 1. A telescope collects the light from the distant SC and interferes it with the local beam. The local laser is also interfered with the laser from the adjacent MOSA on the same SC in the local interferometers (TMIs and RFIs). The Gravitational Reference Sensor (GRS) controls the TM relative to the SC in the suspended degrees of freedom.

and are stabilized on a cavity. A total of six lasers are powering 18 interferometers, and enable the TM-to-TM measurement by linear combinations. Per SC, there are two Moving Optical Sub-Assemblies (MOSAs), each attached to a laser source (named “ LA_{ij} ”). They host three interferometers:

- one inter-SC interferometer (ISI) containing the Gravitational Wave (GW) signals,
- one TM-to-SC interferometer (TMI), used to monitor the reference points in this split interferometry setup, and

- one reference interferometer (RFI), used for laser locking and reduction of common noise.

Between the two SC of one LISA arm, there are two symmetric laser links. Due to divergence of the Gaussian output beam, the laser power reduces drastically over the 2.5 Gm propagation distance to a few hundreds pW at the receiving SC; it is then interfered with a local mW beam. The laser beams will carry additional modulation sidebands used for clock synchronization, ranging information and data transfer, which further reduce the available power in the main carrier-to-carrier beat signal to about 81% [1, 12].

The two adjacent MOSAs exchange their laser light via fiber backlinks, see Fig. 2. To reduce backscatter, the powers guided into the fibers are also relatively small (in the order of mW to nW) and are interfered with beams a few orders of magnitude stronger, such that the beam power ratio in any interferometer is far from unity. By design, the laser beam properties in each interferometer are different. Even comparing the two local interferometers between each MOSA on a single SC, which receive beams from the same laser source and share the same absolute beat frequency, shows that they have their power ratios inverted due to the fiber transfer; thus the local SC scaling of the RIN-to-phase couplings (that depend on the power ratios for 1f-RIN) are not completely identical, as will be considered later in this article.

In every interferometer, two beams interfere at a recombination beamsplitter and PDs measure their impinging time-varying power. The two output ports of each of these beamsplitters are used to apply balanced detection to the (naturally π -shifted) signals, which allows us to subtract both ports to reduce noises like 1f-RIN, while maintaining the signal information [10].

The phase measurement is performed by dedicated Digital Phase-Locked Loops (DPLLs) [13, 14], as depicted in Fig. 3. The loops are able to track the time-varying beatnote over many MHz and measure the phase with μ -cycle precision. It resembles a typical I/Q-demodulation scheme, but is all performed digitally and uses a control loop on the Q quadrature as an error signal for an Numerically Controlled Oscillator (NCO) to drive the mixing process.

Since each laser is involved in 6 interferometers, they can possibly add correlated noise in those interferometers. However, the RIN-to-phase coupling depends on the absolute beat frequency (and its harmonic), which means that RINs at different heterodyne frequencies in different interferometers can be considered uncorrelated if the beatnote frequencies are reasonably well separated, i.e., by more than the measurement band of a few Hz; this holds even if the same laser is involved. RIN from different laser sources is always considered uncorrelated, especially at MHz frequencies. This means that RIN in the TMIs and RFIs on the same SC is correlated, while the Inter-Spacecraft Interferometers (ISIs) may not have correlations. Furthermore, the ISIs are subject to orbital Doppler shifts (in the MHz range) and thus their hetero-

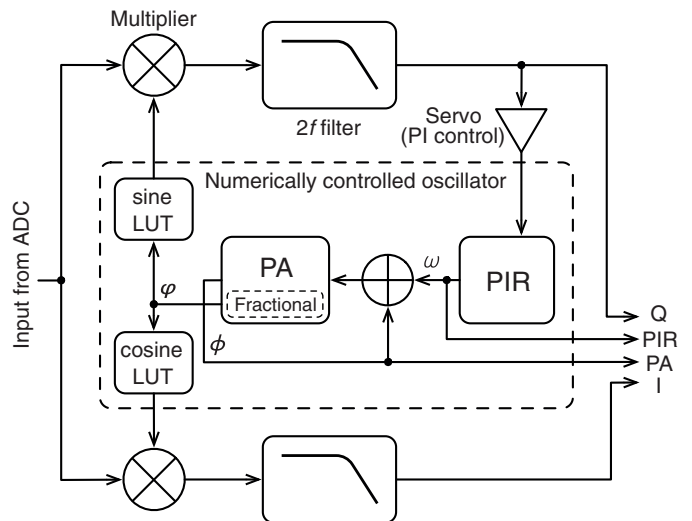


FIG. 3. Schematic of a DPLL in LISA. The input time series from the ADC is mixed with the sine from an NCO, which represents a closed control loop with the down-mixed instantaneous frequency as its error signal. The DPLL is able to follow the input frequency (even for time-varying heterodyne frequencies) within its bandwidth and accumulates the total phase of the input, which is the desired phase measurement. PA phase accumulator; PIR phase-increment register; LUT look-up table; PI proportional-integral. Reprint from [14].

dyne frequencies vary. The expected shifts can be calculated beforehand and are used to enable and optimize the interferometry and detection process. The absolute beat frequencies are technically restricted to a range of approximately (5 to 25) MHz via an (offset) frequency locking scheme of the lasers. This results in a configuration where one primary laser is locked to a cavity, while the other five lasers are locked (with MHz offsets) to the primary laser. The required offset frequencies are calculated on ground, yielding a so-called frequency plan. Various possible locking topologies (with LA₁₂ as the primary laser) have been identified [12, 15], as shown in Fig. 4.

The locking also inevitably imprints any noise (and signal) information of the interferometers used for locking onto the locked lasers. Therefore, RIN-induced phase noise will also be added to the locked laser and propagates through the constellation into all six interferometers of that laser. Furthermore, the next laser that locks on the first locked laser will continue to carry this noise and thus have locally increased phase noise.

Figure 5 shows one possible schematic for the local laser control loop used for locking. Here, we assume that the error signal of the control loop has been balanced between the two interferometer output ports (current baseline), which propagates only a reduced amount of phase noise “echos” through the constellation.

We calculate and simulate these effects in this paper. Luckily, TDI strongly suppresses any laser phase fluctuations in post-processing, including echoes from the locking control loops, such that the final TDI variables are

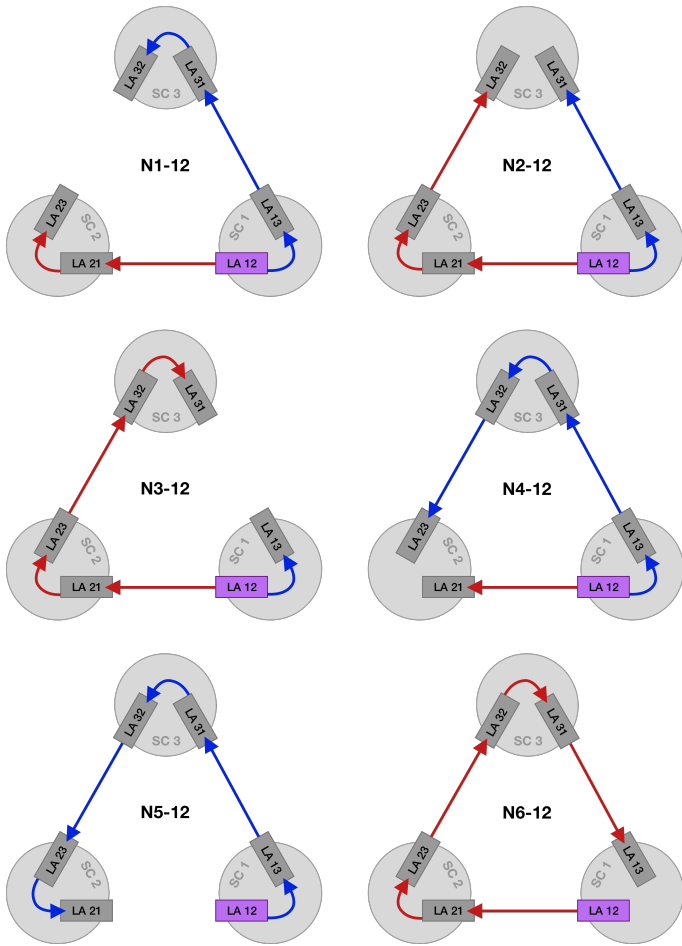


FIG. 4. Schematic of the different locking configurations, here with laser LA_{12} as the primary laser. Reprint from [12].

unaffected by the choice of the locking topology [9, 12].

III. RIN COUPLING IN LISA

The RIN $n = P(t)/\langle P(t) \rangle$ of any laser power $P(t)$, usually expressed in Amplitude Spectral Density (ASD) units of $1/\sqrt{\text{Hz}}$, causes phase noise in the interferometric readout via three distinct coupling channels [4, 10]. First, “DC-RIN” inside the measurement band at low frequencies causes slow intensity fluctuations that lead to radiation pressure on the SCs (negligible) and TMs (not negligible). This drives the low-frequency RIN requirements and has an assumed level of $100 \text{ ppm}/\sqrt{\text{Hz}}$ at 0.1 mHz . It gives a small contribution to the TM acceleration of about $0.35 \text{ fm/s}^2/\sqrt{\text{Hz}}$, out of a total acceleration noise allocation of roughly $10 \text{ fm/s}^2/\sqrt{\text{Hz}}$ at 0.1 mHz [1].

Secondly, 1f-RIN from around the heterodyne frequency causes additive phase noise to the main signal on the PDs.

Finally, 2f-RIN from around twice the heterodyne frequency is optically down-mixed and also produces addi-

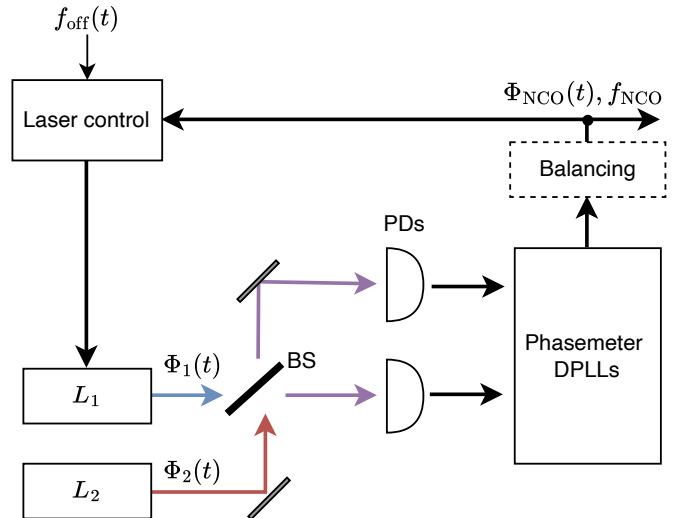


FIG. 5. Schematic of the outer offset frequency locking control loop with DPLLs. This represents the simplified view of one LISA interferometer, which is used for locking laser L_1 to laser L_2 with a typical bandwidth of multiple kHz. The two lasers with phase evolution $\Phi_i(t)$ are brought to interference via the BS, detected on the PDs (in reality redundant QPDs) and measured in the phasemeter. The instantaneous (balanced) frequencies of the DPLL are used to offset lock the lasers according to the predetermined frequency planning.

tive noise (to first order) at the heterodyne frequency.

We focus in this article on the latter two mechanisms. They do not cause any direct force noise, and therefore do not generate any real TM motion signal, but cause an additive small-vector readout noise instead.

Since the RIN is a property of the laser beams, it appears correlated on all QPD segments of a single diode. In this paper, we use the terms QPD and PD interchangeably, as it has no impact on our description of the RIN coupling in the longitudinal degree of freedom.

A. Theory of DPLL readout

In the next sections, we derive the RIN-to-phase coupling equations using the LISA-specific DPLL readout architecture.

The DPLL depicted in Fig. 3 is a control loop that uses the error signal, Q , to adjust the total phase and frequency of an NCO. Contrary to a simple I/Q demodulation, the phase readout is not directly given by combining the I/Q channels, but instead available by digitally reading out the NCO registers.

When the loop is closed, and if we assume it to work perfectly with infinite gain in the measurement band, the error signal will be exactly equal to zero. The error signal is produced by multiplying the incoming signal (modeled as a cosine) by a sine that is perfectly in phase.

We consider an input signal that has a strong main

beatnote plus small additive disturbing terms, representing small-vector RIN. We write

$$V(t) = A \cos(\Phi(t)) + n(t), \quad (3)$$

where we assume A to be constant, and $|n(t)| \ll A$. Here, $\dot{\Phi}(t)$ is typically in the order of MHz. $n(t)$ represents our different RIN terms, but could in principle also be any other additive noise.

We assume that the phase error caused by the disturbance $n(t)$ is small, of order $\ll 1$ expressed in cycles or radian. Therefore, we consider the NCO signal used in the lock to closely follow the main beatnote, and model it as

$$U(t) = \sin(\Phi(t) + \varphi(t)), \quad (4)$$

where $\varphi(t) \ll 1$ accounts for the phase readout errors due to the disturbance $n(t)$. The total phase

$$\Phi_{\text{NCO}}(t) = \Phi(t) + \varphi(t) \quad (5)$$

represents our phase readout and is available from the phasemeter phase accumulator.

The error signal is then computed by mixing the NCO signal with the input signal,

$$Q(t) = \langle V(t)U(t) \rangle, \quad (6)$$

where $\langle \cdot \rangle$ denotes a low-pass filter removing frequency content far away from DC. We assume that this filter is a linear operation, in the sense that $\langle aX + bY \rangle = a\langle X \rangle + b\langle Y \rangle$. A typical example for such a filter is a moving average.

The loop will adjust the phase of the NCO to drive the error signal to zero. This means we can model how the disturbance $n(t)$ affects the output of the DPLL for the closed loop by solving the equation $Q \equiv 0$ for φ ; i.e., by finding the NCO phase for which the error signal vanishes.

B. Phase readout

Combining the previous equations, we can write

$$Q = \langle A \cos(\Phi(t)) \sin(\Phi(t) + \varphi(t)) \rangle + \langle n(t) \sin(\Phi(t) + \varphi(t)) \rangle. \quad (7)$$

Using trigonometric identities and that $\varphi(t) \ll 1$, the first term on the right-hand side

$$\langle A \cos(\Phi(t)) \sin(\Phi(t) + \varphi(t)) \rangle \approx \frac{A}{2} \varphi(t). \quad (8)$$

To treat the other term, we first expand to first order in φ and then neglect the second-order term containing

$\varphi(t)n(t)$, yielding

$$\langle n(t) \sin(\Phi(t) + \varphi(t)) \rangle \approx \langle n(t) \sin(\Phi(t)) \rangle. \quad (9)$$

Using this in Eq. (7), with the locking condition $Q \equiv 0$, gives the phase error induced by $n(t)$,

$$\varphi(t) \approx -\frac{2}{A} \langle n(t) \sin(\Phi(t)) \rangle, \quad (10)$$

and the total phase readout will be given as

$$\Phi_{\text{NCO}}(t) \approx \Phi(t) - \frac{2}{A} \langle n(t) \sin(\Phi(t)) \rangle. \quad (11)$$

This means that, to first order, the disturbance is simply mixed with the main beatnote and scaled by the reciprocal beatnote amplitude.

C. Scaling for RIN

We now need to apply Eq. (11) to the typical photodiode detection equations adapted for heterodyne interferometry. They provide the scaling factors for A and $n(t)$ that describe the RIN coupling correctly. The equations are derived in [10], and are given here with the relevant RIN terms only. Note that any input DC contributions are neglected here. We use the equations adapted for LISA to describe the interferometer output ports A and B of the recombination beamsplitter (with amplitude transmission and reflection coefficients τ, ρ , average beam powers P_i , heterodyne efficiency η_{het} , and RIN n_m, n_r for a general measurement and general reference beam m, r and a certain signal power in the carrier of $\epsilon_{\text{carrier}}$). They yield, for the measured powers per output port,

$$P_A = \underbrace{\rho^2 P_m n_m + \tau^2 P_r n_r}_{\text{1f-RIN, port A}} + \underbrace{(n_m + n_r) \rho \tau \epsilon_{\text{carrier}} \sqrt{\eta_{\text{het}} P_m P_r} \cos(\Phi(t))}_{\text{2f-RIN, port A}} + \underbrace{2 \rho \tau \epsilon_{\text{carrier}} \sqrt{\eta_{\text{het}} P_m P_r} \cos(\Phi(t))}_{\text{Signal, port A}}, \quad (12)$$

and

$$P_B = \underbrace{\tau^2 P_m n_m + \rho^2 P_r n_r}_{\text{1f-RIN, port B}} - \underbrace{(n_m + n_r) \rho \tau \epsilon_{\text{carrier}} \sqrt{\eta_{\text{het}} P_m P_r} \cos(\Phi(t))}_{\text{2f-RIN, port B}} - \underbrace{2 \rho \tau \epsilon_{\text{carrier}} \sqrt{\eta_{\text{het}} P_m P_r} \cos(\Phi(t))}_{\text{Signal, port B}}. \quad (13)$$

Here, we already see that balanced detection of the form $(P_A - P_B)/2$ is able to suppress 1f-RIN, since it appears with the same sign in both ports. However, 2f-RIN ap-

pears with opposite signs in the two ports, identical to the main signal, and therefore cannot be suppressed by balanced detection.

From these equations we can model the input signal to the DPLL using

$$V(t) = \pm A \cos(\Phi(t)) + a_i n_i(t) \pm \frac{A}{2} n_i(t) \cos(\Phi(t)), \quad (14)$$

with the scale factor $A = 2\rho\tau\epsilon_{\text{carrier}}\sqrt{\eta_{\text{het}}P_mP_r}$, while a_i represents the scale factor for one of the 1f-RIN terms and $n_i(t)$ the RIN of one of the beams. The \pm encodes output port A or B. Since the RIN between the two beams is uncorrelated (as well as 1f- and 2f-RIN per beam), we can calculate their resulting phase noise independently. In terms of spectral densities, one can build their quadratic sum for the total phase noise afterwards.

We assume a relative power stability of the lasers of around $3 \times 10^{-8} \text{ Hz}^{-1/2}$ in the relevant bandwidth, such that the resulting phase noise will be small, $\varphi(t) \ll 1$. This allows to use the previous result of Eq. (10).

Therefore, we insert $n(t) = a_i n_i(t) \pm \frac{A}{2} n_i(t) \cos(\Phi(t))$ into Eq. (10), which gives for the resulting phase noise (generated by one laser beam $i = m, r$),

$$\varphi_i(t) = -\underbrace{\frac{2a_i}{A} \langle n_i(t) \sin(\Phi(t)) \rangle}_{\text{1f-RIN phasenoise}} \mp \underbrace{\frac{1}{2} \langle n_i(t) \sin(2\Phi(t)) \rangle}_{\text{2f-RIN phasenoise}}. \quad (15)$$

We find that the noise $n(t)$ appears mixed both with $\sin(\Phi(t))$ as well as $\sin(2\Phi(t))$. This implies that noise around $\dot{\Phi}(t)$ and $2\dot{\Phi}(t)$ are down-converted to the phasemeter base band and couple into the phase accumulator. Due to the down- and up-conversion process of the mixing, only half of that noise power is actually contributing to $\varphi(t)$, since the other half is filtered out. We also see that the 2f-RIN is independent of the signal amplitude or average beam powers.

The total RIN-to-phase coupling must contain the RIN from both beams,

$$\varphi_{\text{tot}}(t) = \varphi_m(t) + \varphi_r(t), \quad (16)$$

with the corresponding coupling factors $a_m = \rho^2 P_m$, $a_r = \tau^2 P_r$ in port A and $a_m = \tau^2 P_m$, $a_r = \rho^2 P_r$ in port B.

After balanced detection, these coupling factors become

$$A = 2\rho\tau\epsilon_{\text{carrier}}\sqrt{\eta_{\text{het}}P_mP_r}, \quad (17)$$

$$a_m = (\rho^2 P_m - \tau^2 P_m)/2, \quad (18)$$

$$a_r = (\tau^2 P_r - \rho^2 P_r)/2. \quad (19)$$

These mixing equations are used in the simulation results presented in later sections to carry over any phase-correlation information correctly. They also agree with the results derived in [10] for a small-vector noise approach, which is slightly less general.

Each interferometer (ISI, TMI, RFI) will carry such a phase error φ_{tot} (here named by interferometer and usually scaled by $\lambda/(2\pi)$),

$$\varphi_{\text{ISI}}(t) = \varphi_{\text{ISI},m}(t) + \varphi_{\text{ISI},r}(t), \quad (20)$$

$$\varphi_{\text{TMI}}(t) = \varphi_{\text{TMI},m}(t) + \varphi_{\text{TMI},r}(t), \quad (21)$$

$$\varphi_{\text{RFI}}(t) = \varphi_{\text{RFI},m}(t) + \varphi_{\text{RFI},r}(t), \quad (22)$$

where the different 1f-RIN amplitudes and total phases depend on the different interferometer optical settings (see Table I).

Note that for our simulations, we do not use Eqs. (18) and (19), but instead model imperfections in the balanced detection by artificially introducing a balancing efficiency, $0 \leq b \leq 1$, and then model the residual 1f-RIN terms as

$$\varphi_{1f,i}(t) = -\frac{2a_i}{A} \langle n_i(t) \sin(\Phi(t)) \rangle \cdot (1-b), \quad (23)$$

while still using perfect 50/50 beamsplitters in the simulation.

D. Simplified phase noise equations without correlations

If only the maximum or RMS RIN-to-phase coupling is required (for example for the noise level in only one interferometer), one can simplify the equations above by dropping the phase information in the mixing process. This ignores correlation properties of RIN but still gives the right level of phase noise per individual interferometer. We use the effect of the filter to select two independent noise series at the in-band sampling frequency. These two time-series $n_{1f}(t), n_{2f}(t)$ have to be scaled due to the mixing and filtering process and represent RIN from around $\dot{\Phi}$ (1f-RIN) and $2\dot{\Phi}$ (2f-RIN). The scale factors arise from simplifying $\langle n(t) \sin(\Phi(t)) \rangle$, which has an ASD of approximately $\frac{1}{\sqrt{2}}\tilde{n}$, with \tilde{n} as the ASD value of $n(t)$.

Therefore, if we want to replace the mixing and filtering process with an in-band, downsampled version of the $n(t)$ noise that has the correct scaling, we can use

$$\langle n(t) \sin(\Phi(t)) \rangle \approx \frac{1}{\sqrt{2}} n_{1f}(t), \quad (24)$$

$$\langle n(t) \sin(2\Phi(t)) \rangle \approx \frac{1}{\sqrt{2}} n_{2f}(t) \quad (25)$$

for the 1f and 2f-RIN terms, respectively. We typically assume $\tilde{n}_{1f} = \tilde{n}_{2f} = 3 \times 10^{-8} \text{ Hz}^{-1/2}$. In total, that gives for one beam

$$\varphi_i(t) \approx -\frac{2a_i}{A} \frac{n_{1f}(t)}{\sqrt{2}} - \frac{1}{2} \frac{n_{2f}(t)}{\sqrt{2}}. \quad (26)$$

The total RIN-induced phase noise from two beams

| Parameter | Value | Description |
|-----------------------------|---|--|
| λ | 1064 nm | Laser wavelength |
| f_{het} | (5 to 25) MHz | Heterodyne frequency |
| $n_{1f, 2f}$ | $3 \times 10^{-8} \frac{1}{\sqrt{\text{Hz}}}$ | Maximum (white) RIN ASD in the band (5 to 50) MHz |
| τ^2, ρ^2 | 0.5 | Beamsplitter (in power when squared as given) transmission and reflection coefficients |
| b | [0.9, 0, 1] | Balancing efficiency, i.e. matching of the 1f-RIN amplitudes in the interferometer ports |
| $\eta_{\text{het,ISI}}$ | 0.75 | Heterodyne efficiency from the overlap integral in a long-arm (ISI) interferometer |
| $\eta_{\text{het,TMI}}$ | 0.82 | Heterodyne efficiency from the overlap integral in a TM (TMI) interferometer |
| $\eta_{\text{het,RFI}}$ | 0.82 | Heterodyne efficiency from the overlap integral in a reference (RFI) interferometer |
| $\epsilon_{\text{carrier}}$ | 0.81 | Portion of power in the carrier of the beams |
| $P_{\text{ISI},1}$ | 350 pW | Mean power of the remote laser in the long-arm interferometer (from distant SC) |
| $P_{\text{ISI},2}$ | 1 mW | Mean power of the local laser in the long-arm interferometer |
| $P_{\text{TMI},1}$ | 500 nW | Mean power of the adjacent laser in the TM interferometer (from adjacent bench) |
| $P_{\text{TMI},2}$ | 500 μ W | Mean power of the local laser in the TM interferometer |
| $P_{\text{RFI},1}$ | 500 nW | Mean power of the adjacent laser in the reference interferometer (from adjacent bench) |
| $P_{\text{RFI},2}$ | 1 mW | Mean power of the local laser in the reference interferometer |
| dx_{SC} | 10 nm/ $\sqrt{\text{Hz}}$ | Residual translational jitter of the SC, with respect to inertial space. When used as a residual path offset in the equations, we calculate a RMS value by integrating over a frequency band from (0 to 1) Hz as in $\sqrt{(10 \text{ nm}/\sqrt{\text{Hz}})^2 \cdot 1 \text{ Hz}} = 10 \text{ nm}$. In LPF we measured a RMS in x_1 of about 2 nm, and a peak-to-peak difference of about 10 nm |
| ϕ_{ISI} | dx_{SC} | Without noises or signals the measured phase due to minimal residual translational jitter in an ISI |
| ϕ_{TMI} | $dx_{\text{SC}}, [-2\pi, 2\pi]$ | Limit of TMI interferometer set-point due to residual jitter or TM guidance injection |
| ϕ_{RFI} | 0 rad | RFI interferometer phase offset |

TABLE I. Parameters of the optical chain with special relevance for the RIN to phase coupling. Where multiple numbers are stated they correspond to the different simulations performed. The values are estimates from current design studies, and are subject to minor changes.

would then be the same sum as before, $\varphi_{\text{tot}}(t) = \varphi_m(t) + \varphi_r(t)$, but now expressed simply by four uncorrelated noise time series with low sampling frequency and corresponding standard deviation. This can be used to set upper boundaries per interferometer level or for the locally correlated measurements (by using correlated time series for upper-boundary estimates).

E. Laser locking

The required control for laser locking adds another outer loop that uses the instantaneous frequency measured by the inner DPLL, as depicted in Fig. 5. Each laser has its own phase, $\Phi_1(t), \Phi_2(t)$, such that the beatnote is represented by the total difference phase $\Phi(t) = \Phi_1(t) - \Phi_2(t)$. As before, we denote by $n(t)$ an additive noise source, in our case RIN.

From the locking condition of the DPLL, Eq. (11), we know that

$$\Phi_{\text{NCO}}(t) \approx \Phi(t) - \frac{2}{A} \langle n(t) \sin(\Phi(t)) \rangle.$$

The outer offset frequency locking loop has the (ideal

in-band) locking condition that

$$f_{\text{NCO}}(t) - f_{\text{off}}(t) \equiv 0, \quad (27)$$

$$\iff \dot{\Phi}_{\text{NCO}}(t) - f_{\text{off}}(t) \equiv 0 \quad (28)$$

where the frequency offsets $f_{\text{off}}(t)$ are predefined values calculated from the frequency planning.

This locking is assumed to be perfect (in the measurement band, within a bandwidth of ~ 10 kHz), such that any disturbance of the offset phase, for example due to RIN, laser frequency noise, or even gravitational-wave signals, is added sign-inverted to the laser phase (compared to the phasemeter measurement). This implies that any of those terms cancel in the respective interferometer. Note that we assume the current baseline, i.e., that the locking will use the balanced readout, such that 1f-RIN is already minimized at the input to the control loop and therefore not fully imprinted on the laser, and thus not canceled on the level of individual photodiodes. Since 2f-RIN is not canceled by balanced detection, it will be fully imprinted on the laser, i.e., it will be fully canceled on the level of individual photodiodes.

We can see this easily if we look at the outer loop locking equation. In the phase domain, after integrating Eq. (27) and setting the integration constant to 0, we

have

$$0 \equiv \Phi_{\text{NCO}}(t) - \Phi_{\text{off}}(t) \quad (29)$$

$$\Rightarrow \Phi_{\text{off}}(t) \approx \Phi(t) - \frac{2}{A} \langle n(t) \sin(\Phi(t)) \rangle \quad (30)$$

$$\Leftrightarrow \Phi_{\text{off}}(t) \approx \Phi_1(t) - \Phi_2(t) - \frac{2}{A} \langle n(t) \sin(\Phi_1(t) - \Phi_2(t)) \rangle \quad (31)$$

$$\Rightarrow \Phi_1(t) = \Phi_2(t) + \Phi_{\text{off}}(t) + \frac{2}{A} \langle n(t) \sin(\Phi_1(t) - \Phi_2(t)) \rangle. \quad (32)$$

We see that the equation is implicit and cannot be solved analytically for $\Phi_1(t)$. We can iteratively solve it to first order,

$$\Phi_1(t) = \Phi_2(t) + \Phi_{\text{off}}(t) + \frac{2}{A} \langle n(t) \sin([\Phi_1(t) = \dots] - \Phi_2(t)) \rangle \quad (33)$$

$$\approx \Phi_2(t) + \Phi_{\text{off}}(t) + \frac{2}{A} \langle n(t) \sin(\Phi_{\text{off}}(t)) \rangle \quad (34)$$

$$\approx \Phi_2(t) + \Phi_{\text{off}}(t) + \frac{2}{A} \langle n(t) \sin(\Phi(t)) \rangle. \quad (35)$$

We expect that the effect of the loop on the input signal $\Phi_1(t)$ is very small due to $n \ll 1$, which allows the approximations in the last two equations for simulation purposes. It is assumed here that the loop will always have enough bandwidth to perfectly cancel the measured noise and imprint it on the laser phase, “echoing” it through the constellation.

As an example, we give the locking propagation equations for the baseline N1-12 locking configuration, see [Fig. 4](#); laser phase is locked with the phase error measured in the respective locking interferometer, and propagated with delays such that the laser phase errors can be written as

$$R_{12} = \text{Reference}, \quad (36)$$

$$R_{13} = \text{sign}(t_{13}) \cdot t_{13}, \quad (37)$$

$$R_{31} = \text{sign}(s_{31}) \cdot s_{31} + D_{31}(R_{13}), \quad (38)$$

$$R_{32} = \text{sign}(t_{32}) \cdot t_{32} + R_{31}, \quad (39)$$

$$R_{21} = \text{sign}(s_{21}) \cdot s_{21}, \quad (40)$$

$$R_{23} = \text{sign}(t_{23}) \cdot t_{23} + R_{21}, \quad (41)$$

where R_{ij} describes the RIN phase error that each laser LA_{ij} is carrying. The shorthand notation t_{ij} stands for the RIN phase error originating from RFI_{ij} and s_{ij} maps the RIN phase error from ISI_{ij} . Delays D_{ij} are defined as in [Fig. 1](#) and the $\text{sign}(\cdot)$ represents the sign of the beat frequency in the corresponding interferometer.

F. RIN Correlations in LISA

In this section, we discuss possible correlations between interferometers.

First, between the two ISIs where the same laser is involved, a potential short-time correlation can appear if the beatnote frequencies are identical at the times the measurements are combined in TDI, i.e., at multiples of the light travel time between the SC. This is very unlikely to happen due to the frequency planning and the arm-breathing.

In any case, the overall RIN contributions in the ISIs will be completely dominated by the RIN of the local beam, due to the power ratios $\sqrt{P_{\text{ISI},1}/P_{\text{ISI},2}} \cdot n_{1f}(t) \ll \sqrt{P_{\text{ISI},2}/P_{\text{ISI},1}} \cdot n_{1f}(t)$. Thus, any potential correlation would involve one of the negligible terms, and can therefore be safely ignored.

Second, as explained before, 1f-RIN and 2f-RIN are several MHz apart due to the mission design, and thus can be considered as uncorrelated. However, the same two lasers interfere in the four local TMIs and RFIs on each SC and therefore produce correlated RIN. The correlation (1f- with 1f-RIN) is not very strong, since the power ratios are inverse in the local interferometers of two adjacent MOSAs. In the case of 2f-RIN, there is full correlation, since it does not depend on the beam powers.

Third, we consider possible correlations between the 2 ISIs and the 4 remaining interferometers on one SC. To minimize crosstalk in the DPLL, the frequency plan ensures that the RFIs/TMIs and the ISIs on one SC do not share the same heterodyne frequency, with a margin of about 2 MHz. Therefore, no direct correlations are expected to occur. The remaining possibility is for correlations between 1f- and 2f-RIN, e.g., if one beat is at 12 MHz and the other one at 6 MHz. This would lead to a correlation between 1f-RIN from the 12 MHz beat with 2f-RIN in the 6 MHz beat. However, this can be considered unproblematic, here again, as the 1f-RIN term is likely to be dominating. In addition, such a scenario is a rare event: even with a relatively large threshold of 50 Hz difference between the beats (compared to the ~ 4 Hz measurement band), the maximal duration involving correlated measurements across all lasers and interferometers is in the order of a few hours for over 10 years of simulated frequency plan data (shown in [Fig. 6](#) for the baseline N1-L12 configuration). Furthermore, the frequency plan could be further optimized to avoid such crossings, if desired.

G. Influence of TDI

TDI strongly suppresses laser phase noise by about 8 orders of magnitude. For this purpose, it uses time shifted combinations of the interferometric phase measurements. As such, it also suppresses the laser locking noise “echos”, since they appear in the measurements identically to the laser frequency noise that TDI is de-

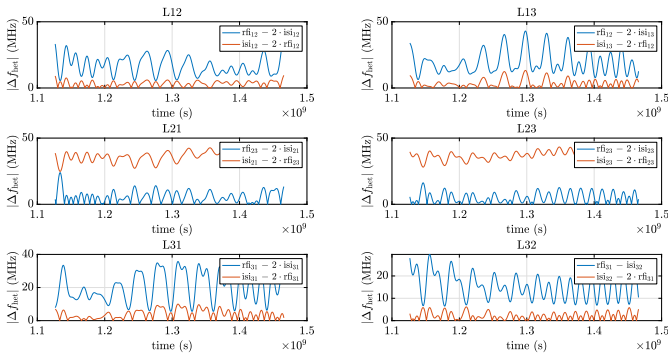


FIG. 6. Locking beatnote differences between local and ISI interferometers per laser. It shows the possibility of 1f-2f-RIN correlations for the baseline configuration N1-12 for more than 10 years of data. We show pairwise absolute beat frequency differences for each laser. Only when the difference is becoming as small as a few Hz, the correlation would show up in the data. This only happens for a few hours in total for all lasers per configuration for the whole duration of more than 10 years and causes negligible extra phase noise. The frequency plan considered here is computed for Earth-trailing orbits provided by ESA.

signed to suppress. Unfortunately, this process also adds other noises from the 18 interferometric measurements into the resulting TDI variables. These noises have been studied and are now well understood (see, for example, [9]). To first order, RIN can be considered to behave like any other uncorrelated readout noise due to its properties discussed before; especially since the most significant RIN contribution appears uncorrelated in the ISIs, while the correlated appearances (TMI, RFI) produce much smaller noise contributions to the total measurement chain. According to [9], an uncorrelated readout noise (e.g., in units of $m/\sqrt{\text{Hz}}$) entering all ISIs with a level of $\tilde{\varphi}$, which describes the dominant RIN contribution, has a Power Spectral Density (PSD) in the TDI combination X_2 of

$$S_{X_2}(\omega, \tilde{\varphi}) = 4\tilde{\varphi}^2 C_{XX}(\omega), \quad (42)$$

$$C_{XX}(\omega) = 16 \sin^2\left(\omega \frac{L}{c}\right) \sin^2\left(\omega \frac{2L}{c}\right), \quad (43)$$

where $\omega = 2\pi f$, and c is the speed of light in a vacuum.

IV. SIMULATION ARCHITECTURE

To verify the validity of the analytical derivations presented in the previous section and track the effects of possible correlations, we implemented a time-domain simulation.

Figure 7 gives an overview of this simulator, which has multiple stages and is able to simulate the whole LISA constellation with its 18 interferometers. The simulation is performed in phase domain to easily represent

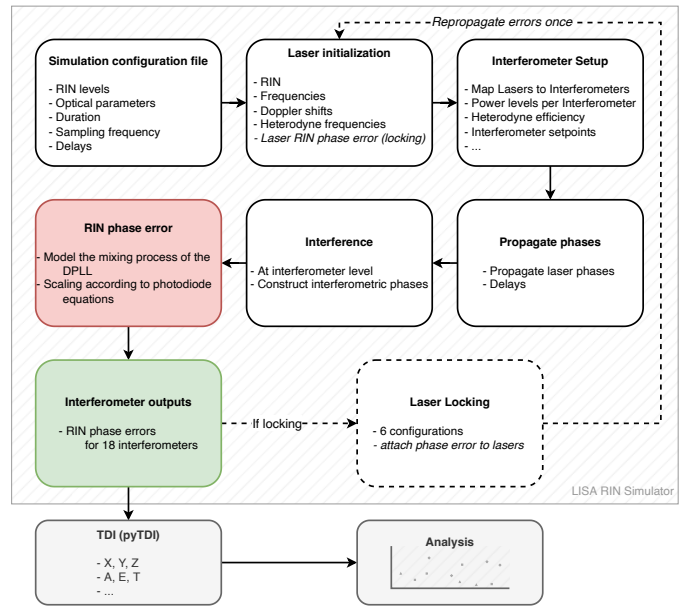


FIG. 7. Diagram to show the different stages of the RIN simulation.

the mixing process inside the DPLL. The laser and optical parameters are read from a configuration file and then propagated to the interferometers, where the interference phase of two beams is simulated. Then, the RIN phase error due to the mixing and demodulation process is calculated at high sampling frequency, and used as an output either for the locking scheme or directly for the output of the interferometers. Consecutive scripts perform the data analysis tasks.

Typically, we simulate tens of thousands of seconds with a sampling frequency of 1 kHz.

We simulate the total phase of each interferometer. Since we cannot simulate MHz frequencies directly for long time periods, we choose the offset frequencies such that all beatnote frequencies are in a range between 100 Hz and 250 Hz, instead of 5 MHz and 25 MHz. This is sufficient to accurately model the RIN coupling in the time domain, as its behavior is independent of the absolute heterodyne frequency.

We simulate laser locking, and correctly keep track of the beatnote polarities. The locking control loop is assumed to be perfect, such that the locking interferometer error signal is sign-inverted and added to the locked laser, and then propagates to all interferometers involving this laser.

Following previous considerations for the frequency planning, we assume that only local interferometers on the same SC share the same heterodyne frequency. Additionally, each laser carries its own RIN noise time series, which is propagated (and delayed where applicable) to the corresponding interferometers.

The delays, in the order of 8 s, are constant and symmetric for the two directions of each arm, but not equal between different arms. The initial assumption of un-

equal beatnote frequencies would not be violated for slowly-varying arm lengths due to the frequency locking, as explained above. This is especially valid for our relatively short simulations, for which the frequencies do not change much.

The RIN mixing is then applied using all beatnote phases and corresponding lasers with their RIN time series. We include a model for balanced detection with different balancing efficiencies. The RIN phase error is propagated as its own time series through the constellation, to avoid numerical problems with the large phase ramps of the beatnote phases. The outputs are filtered and downsampled, typically to a final output sampling frequency of 10 Hz.

V. RESULTS

In this section, we present our analytical and simulated results for the LISA mission parameters. The main findings are summarized in [Table II](#), [Fig. 8](#) and [Fig. 10](#). We show the expected noise levels per interferometer, local common-mode suppression, and the propagation through TDI.

A. 1f-RIN estimates

Based on the theoretical derivation above (and [\[10\]](#)) and the optical parameters relevant for the RIN-to-phase coupling from the current LISA design (given in [Table I](#)), we estimate the expected noise levels in the three distinct interferometers without locking.

The 1f-RIN couplings are strong contributors to the phase noise in LISA. The TMI shows a 1f-RIN contribution of about $155 \text{ fm}/\sqrt{\text{Hz}}$, the RFI has a noise of about $220 \text{ fm}/\sqrt{\text{Hz}}$ and the ISI reaches even a level of $8.7 \text{ pm}/\sqrt{\text{Hz}}$. Assuming a balancing efficiency of 90%, these values reduce to $15.5 \text{ fm}/\sqrt{\text{Hz}}$, $22 \text{ fm}/\sqrt{\text{Hz}}$, and $0.87 \text{ pm}/\sqrt{\text{Hz}}$. The correlated TMI – RFI subtraction in TDI is able to reduce the contribution of these two interferometers to about $6.5 \text{ fm}/\sqrt{\text{Hz}}$. Contrary to the results presented in [\[10\]](#), a complete subtraction is not possible in LISA due to the unequal beam powers in the correlated interferometers, even if the residual translational SC jitter dx_{SC} vanishes.

In total, we get for a single link (uncorrelated ISI, two uncorrelated TMI – RFI measurements) $\sqrt{(0.87 \text{ pm}/\sqrt{\text{Hz}})^2 + (\sqrt{2} \cdot 6.5 \text{ fm}/\sqrt{\text{Hz}})^2}$, that is approximately $0.87 \text{ pm}/\sqrt{\text{Hz}}$.

B. 2f-RIN estimates

We find white-noise baseline estimates for 2f-RIN of about $2.5 \text{ fm}/\sqrt{\text{Hz}}$ in the ISI, TMI and RFI. This value

is expected to be identical across the interferometers, because the coupling is independent of beam parameters, such as powers. Since it is correlated in the TMI – RFI subtraction performed in TDI, the contribution of these two interferometers is further reduced by a similar sine factor (with twice its argument) as the 1f-RIN only adds marginal noise to the single link TM-to-TM measurement [\[10\]](#). Here, full subtraction is possible, since the noise in the correlated interferometers does not depend on the beam powers.

The total 2f-RIN noise in a single TM-to-TM link can be estimated by $\sqrt{(2.5 \text{ fm}/\sqrt{\text{Hz}})^2 + (\sqrt{2} \cdot 0.3 \text{ fm}/\sqrt{\text{Hz}})^2} \approx 2.6 \text{ fm}/\sqrt{\text{Hz}}$. Therefore, the phase noise due to 2f-RIN is much weaker than the phase noise caused by 1f-RIN.

C. Differential Wavefront Sensing (DWS)

DWS uses pairs of photodiode quadrants to sense wavefront tilts between the measurement and reference beams. It is used for SC and TM angular control, since the wavefront tilts can be calibrated to yield physical TM-to-SC angles. As such, it uses the same phase readout (yet different quadrant combinations, see for example [\[14\]](#)) as the longitudinal channels and will therefore also be affected by RIN. The behavior is expected to be the same as in the longitudinal TMI – RFI common mode suppression (because pairs of quadrants are always combined), but with better results due to effectively equal power levels across the quadrants. Since the expected angles measured through DWS are rather small (usually less than 1 rad for the non-calibrated quadrant phase) and the quadrants share the same correlated RIN, common-mode suppression, together with balanced detection, are expected to yield good minimization effects.

D. Contribution summary

In total, we find the quadratic sum of the 1f-RIN and 2f-RIN contributions for a single TM-to-TM link, with 90% balancing efficiency and no laser locking, to be at a level of $0.87 \text{ pm}/\sqrt{\text{Hz}}$ for the longitudinal readout. This amount of noise has to be considered as an entry in the $\sim 10 \text{ pm}/\sqrt{\text{Hz}}$ noise budget of the total optical metrology noise. Let us note how important it is that the balancing requirements are met; if not, the total optical metrology budget would already be dominated by the RIN-induced phase noise.

More detailed estimates are given in [Table II](#) as a summary of the expected noise ASD levels per local interferometer and the biggest local noise measurements for all locking schemes, based on the parameters of [Table I](#). These have been calculated both analytically (where directly possible) and numerically simulated using the RIN simulator described above, where we disabled all other

| Locking config. | Interferometer | 1f-RIN | 2f-RIN | Total ($b = 0.9$) | Total ($b = 1$) | Total ($b = 0$) |
|-----------------|---------------------------------------|------------------------|-----------------------|------------------------|-----------------------|------------------------|
| None | ISI _{ij} | 8.7×10^{-12} | 2.5×10^{-15} | 0.87×10^{-12} | 2.5×10^{-15} | 8.7×10^{-12} |
| | TMI _{ij} | 0.16×10^{-12} | 2.5×10^{-15} | 16.2×10^{-15} | 2.5×10^{-15} | 0.16×10^{-12} |
| | RFI _{ij} | 0.22×10^{-12} | 2.5×10^{-15} | 22.2×10^{-15} | 2.5×10^{-15} | 0.22×10^{-12} |
| | TMI _{ij} - RFI _{ij} | 65.6×10^{-15} | 3.0×10^{-16} | 6.5×10^{-15} | 3.0×10^{-16} | 65.6×10^{-15} |
| N1-12 | ISI ₃₂ | | | 1.5×10^{-12} | 6.2×10^{-15} | 15.0×10^{-12} |
| | ISI ₂₃ | | | 1.5×10^{-12} | 6.2×10^{-15} | 15.0×10^{-12} |
| | ISI ₁₃ | | | 1.2×10^{-12} | 5.1×10^{-15} | 12.3×10^{-12} |
| N2-12 | ISI ₂₃ | | | 1.7×10^{-12} | 6.2×10^{-15} | 17.4×10^{-12} |
| | RFI ₃₂ | | | 1.5×10^{-12} | 6.2×10^{-15} | 15.0×10^{-12} |
| | RFI ₃₁ | | | 1.5×10^{-12} | 6.2×10^{-15} | 15.0×10^{-12} |
| N3-12 | ISI ₂₃ | | | 1.7×10^{-12} | 6.2×10^{-15} | 17.4×10^{-12} |
| | ISI ₁₃ | | | 1.5×10^{-12} | 6.2×10^{-15} | 15.0×10^{-12} |
| | ISI ₃₁ | | | 1.5×10^{-12} | 6.2×10^{-15} | 15.0×10^{-12} |
| N4-12 | ISI ₃₂ | | | 1.7×10^{-12} | 7.2×10^{-15} | 17.4×10^{-12} |
| | RFI ₂₁ | | | 1.5×10^{-12} | 6.2×10^{-15} | 15.0×10^{-12} |
| | RFI ₂₃ | | | 1.5×10^{-12} | 6.2×10^{-15} | 15.0×10^{-12} |
| N5-12 | ISI ₃₂ | | | 1.7×10^{-12} | 7.2×10^{-15} | 17.4×10^{-12} |
| | ISI ₂₁ | | | 1.5×10^{-12} | 6.2×10^{-15} | 15.0×10^{-12} |
| | ISI ₁₂ | | | 1.5×10^{-12} | 6.2×10^{-15} | 15.0×10^{-12} |
| N6-12 | ISI ₃₁ | | | 2.1×10^{-12} | 8.0×10^{-15} | 21.2×10^{-12} |
| | ISI ₂₃ | | | 1.7×10^{-12} | 6.2×10^{-15} | 17.3×10^{-12} |
| | RFI ₁₃ | | | 1.5×10^{-12} | 6.2×10^{-15} | 15.0×10^{-12} |

TABLE II. Numerical simulation of the RIN-to-phase coupling in various interferometers, based on the parameters listed in Table I. The first four rows show the resulting phase noise in the unlocked case. The following rows show the three interferometers with the largest propagated phase noise for each locking configuration. The last columns report the total phase noise assuming different balancing efficiencies (realistic case, best and worst). The laser locking is assumed to be applied to the data after balanced detection with the stated balancing efficiency. The numerical estimates are averages of the flat PSD in the band (0.01 to 2) Hz (using 24 averages and a Blackman-Harris92 window), from 30 000 s of data sampled with 1 kHz each. All values are given in $\text{mHz}^{-0.5}$. The relative standard deviation is of the order of a few %, values are rounded to the last digit.

noises.

0 rad could be chosen to further minimize the noise.

E. Local common-mode rejection

In Fig. 8, we present the local correlated behavior of the frequency-averaged RIN phase error in the TMI_{ij} - RFI_{ij} subtraction. The results follow the expected theoretical pattern (also agrees with Table II) and show the common-mode rejection for a differential phase (labeled TM setpoint here) between the two interferometers. The theoretical pattern is described in [10]. An important observation is that even for the correlated subtraction on the same MOSA, the noise cannot be fully reduced due to the unequal beam powers. Note that this rejection would be even weaker if two interferometers from adjacent optical benches would be used in the subtraction, due to the even more unequal beam powers. Figure 9 shows the measured correlations in this simulation.

Similar effects have been observed in LPF and on ground [10]. During the mission, a set-point close to

F. Propagation through TDI

Having simulated all interferometers with and without locking, the phase outputs need to be propagated through TDI, similar to the real mission data. For this purpose we are using the software package PyTDI [18].

In Fig. 10, we show the results with different balancing efficiencies for the baseline locking configuration (N1-12), and compare these scenarios to the case of unlocked lasers. We also overlay the analytical expectations given below. As expected, we find that TDI suppresses the additional noises due to laser locking, and that the final noise resembles an uncorrelated readout noise, with the transfer function given in Eq. (42). The relevant noise level is given by

$$\tilde{\varphi} = \tilde{\varphi}_{\text{ISI}} \approx (1 - b) \cdot 8.7 \frac{\text{pm}}{\sqrt{\text{Hz}}}, \quad (44)$$

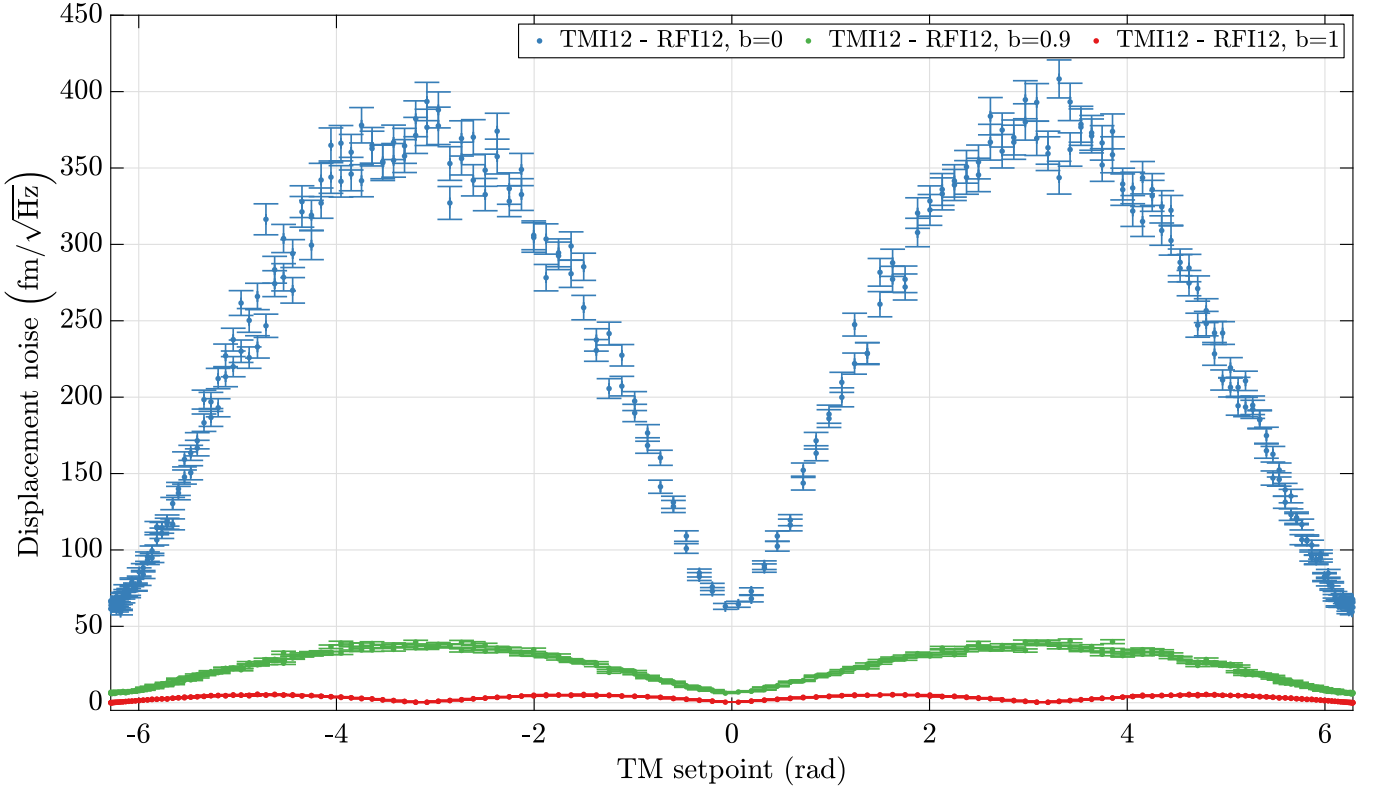


FIG. 8. Simulated data for one local $\text{TMI}_{ij} - \text{RFI}_{ij}$ subtraction with different balancing efficiencies, in the unlocked case. This shows the possible correlation properties of the RIN phase error, following the expected sinusoidal shape. For perfect 1f-RIN subtraction ($b = 1$), only 2f-RIN remains. The different noise floors are due to the unmatched power levels in the two interferometers. For these simulations, a slow sine injection from $[-2\pi, 2\pi]$ has been injected to mimic TM motion for 30 000 s of data sampled at 1 kHz. Each point shown here corresponds to the total measurement having been cut into 100 s segments, and their flat PSDs averaged between 1 and 3 Hz.

with the condition that the ISIs dominate, and $b < 1$. The residual 2f-RIN terms of $2.5 \text{ fm}/\sqrt{\text{Hz}}$ only have to be considered for perfect balanced detection ($b = 1$, see below), when the correlated noise in the TMI and RFI also becomes relevant.

A more detailed (yet still simplified) upper bound for the total noise after TDI can be estimated by adding the transfer function of the individual interferometer contributions, assuming the TMI and RFI add uncorrelated noise only. This leads to $\sqrt{2}$ smaller noise than the maximal possible contribution due to their correlation, but assuming good suppression due to the $\sin(dx_{\text{SC}})$ factor, this would still be a reasonably high upper bound that reduces the required estimation effort drastically. The total RIN propagation after TDI would then follow (using the results from [9]),

$$S_{X_2} = S_{X_2, \text{ISI}} + S_{X_2, \text{TMI}} + S_{X_2, \text{RFI}}, \quad (45)$$

where

$$S_{X_2, \text{ISI}} = 4C_{XX}(\omega) \cdot \tilde{\varphi}_{\text{ISI}}^2, \quad (46)$$

$$S_{X_2, \text{RFI}} = 4C_{XX}(\omega) \cdot \tilde{\varphi}_{\text{RFI}}^2, \quad (47)$$

$$S_{X_2, \text{TMI}} = C_{XX}(\omega) \left(3 + \cos\left(\omega \frac{2L}{c}\right) \right) \cdot \tilde{\varphi}_{\text{TMI}}^2. \quad (48)$$

The noise levels according to the results from the derivation in the previous sections,

$$\tilde{\varphi}_{\text{IFO}} = \frac{\lambda}{2\pi} \sqrt{\left((1-b) \cdot a_{\text{IFO}, 1f} \cdot \tilde{n}_{1f} \right)^2 + \left(\frac{1}{2} \tilde{n}_{2f} \right)^2}. \quad (49)$$

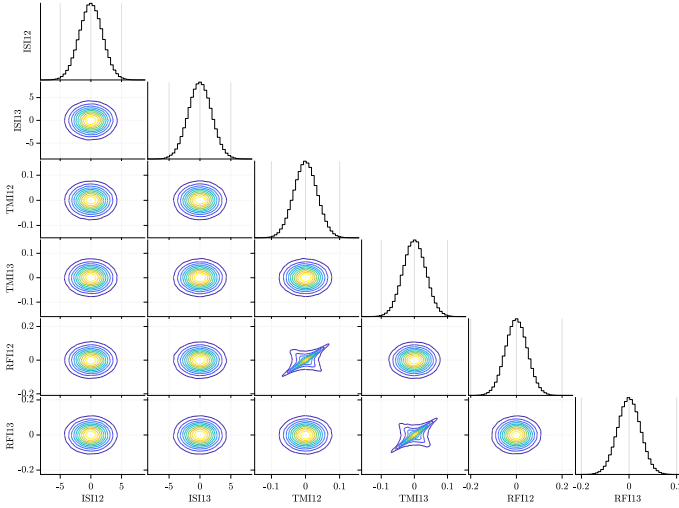


FIG. 9. Correlations between noises of the local interferometers from Fig. 8, here for SC 1, with 90% balancing efficiency and in the unlocked case. The diagonal shows the histogram; off-diagonal elements show density plots with units of picometers. The reason for the slightly rectangular correlations between the local RFI and TMI arises from the mixing process, which contains a sinusoidal multiplication with a phase modulation (the TM setpoint) in this case. We see that the RIN-induced phase noise can be considered largely uncorrelated, even between adjacent local interferometers, due to the inversely distributed powers. The plot has been produced using [16].

This translates for the three distinct interferometers (assuming 50/50 beamsplitters) to

$$a_{\text{ISI},1f} = \frac{1}{\eta_{\text{carrier}}} \sqrt{\frac{P_{\text{ISI},1}^2 + P_{\text{ISI},2}^2}{2\eta_{\text{het,ISI}}P_{\text{ISI},1}P_{\text{ISI},2}}}, \quad (50)$$

$$a_{\text{RFI},1f} = \frac{1}{\eta_{\text{carrier}}} \sqrt{\frac{P_{\text{RFI},1}^2 + P_{\text{RFI},2}^2}{2\eta_{\text{het,RFI}}P_{\text{RFI},1}P_{\text{RFI},2}}}, \quad (51)$$

$$a_{\text{TMI},1f} = \frac{1}{\eta_{\text{carrier}}} \sqrt{\frac{P_{\text{TMI},1}^2 + P_{\text{TMI},2}^2}{2\eta_{\text{het,TMI}}P_{\text{TMI},1}P_{\text{TMI},2}}}, \quad (52)$$

such that we find for the noise levels

$$\tilde{\varphi}_{\text{ISI}} \approx (1-b) \cdot 8.7 \frac{\text{pm}}{\sqrt{\text{Hz}}}, \quad (53)$$

$$\tilde{\varphi}_{\text{RFI}} \approx (1-b) \cdot 220 \frac{\text{fm}}{\sqrt{\text{Hz}}}, \quad (54)$$

$$\tilde{\varphi}_{\text{TMI}} \approx (1-b) \cdot 155 \frac{\text{fm}}{\sqrt{\text{Hz}}}, \quad (55)$$

which is clearly dominated by the ISI terms.

However, in the limit of $b \rightarrow 1$, the 2f-RIN contributions and their correlations become relevant. Then, the RIN residual is expected to be dominated by the sum of uncorrelated contributions in the ISIs and the fully correlated contribution among the local interferometers (TMI and RFI) in the two adjacent MOSAs. This special case

of 2f-RIN correlation is not discussed in the literature, hence we give the derivation here.

If we assign the same noise to all local interferometers on one spacecraft ($\text{RFI}_{ij} = \text{RFI}_{ik} = \text{TMI}_{ij} = \text{TMI}_{ik} = n_{i,2f\text{-RIN}}$) and perform a derivation similar to that presented in [9] (assuming equal arm lengths), we recover the following residual in X_2 ,

$$X_{2,2f\text{-RIN,corr.}} = (1-D^2)^2(1-D^4)\varphi_{1,2f\text{-RIN}}. \quad (56)$$

We note that only the RIN contribution of SC1 remains in X_2 , while those of the other two SC cancel. We compute the PSD by taking the Fourier transform of the previous equation and calculating the expectation value of the squared magnitude, yielding

$$S_{X_2,2f\text{-RIN,corr.}} = 4 \sin^2\left(\omega \frac{L}{c}\right) C_{XX}(\omega) \cdot \tilde{\varphi}_{2f\text{-RIN}}^2, \quad (57)$$

where $\tilde{n}_{2f\text{-RIN}}$ is the equal level of 2f-RIN in all interferometers and the usual TDI transfer function is modulated by an additional sine squared factor. This causes a faster roll-off of the PSD towards low frequencies and is thus only relevant at the maxima of the TDI transfer function. The sum of the uncorrelated ISI RIN $S_{X_2,\text{ISI}}$ term for $b = 1$ and the locally correlated 2f-RIN $S_{X_2,2f\text{-RIN,corr.}}$ term is plotted in Fig. 10 and agrees well with the simulation result.

In a nutshell, the simulated noise coupling propagation through TDI are in very good agreement with the theoretical predictions, and the correlations do not have any significant influence under realistic circumstances.

VI. CONCLUSIONS

We have analyzed, derived, and simulated the RIN-to-phase noise coupling in LISA, a future gravitational-wave observatory in space, and present for the first time a complete analysis of the influence of RIN in the interferometric readout. We have considered the mission characteristics such as laser properties, optical bench design, and orbital dynamic influences, as well as mitigation strategies.

We conclude that the resulting phase noise follows our theoretical understanding and experience from LISA Pathfinder (LPF). It is well under control for the current design parameters of reasonably low input RIN and strong suppression of the dominating 1f-RIN through sufficient balanced detection.

With the mitigation strategies considered here, the RIN phase noise is of the order of $0.87 \text{ pm}/\sqrt{\text{Hz}}$ for the single link TM-to-TM measurement along one LISA arm, and dominated by the 1f-RIN terms in the inter-SC interferometers. The 2f-RIN coupling only plays a subdominant role.

This amount of noise is below other secondary noises that are in the order up to a few $\text{pm}/\sqrt{\text{Hz}}$.

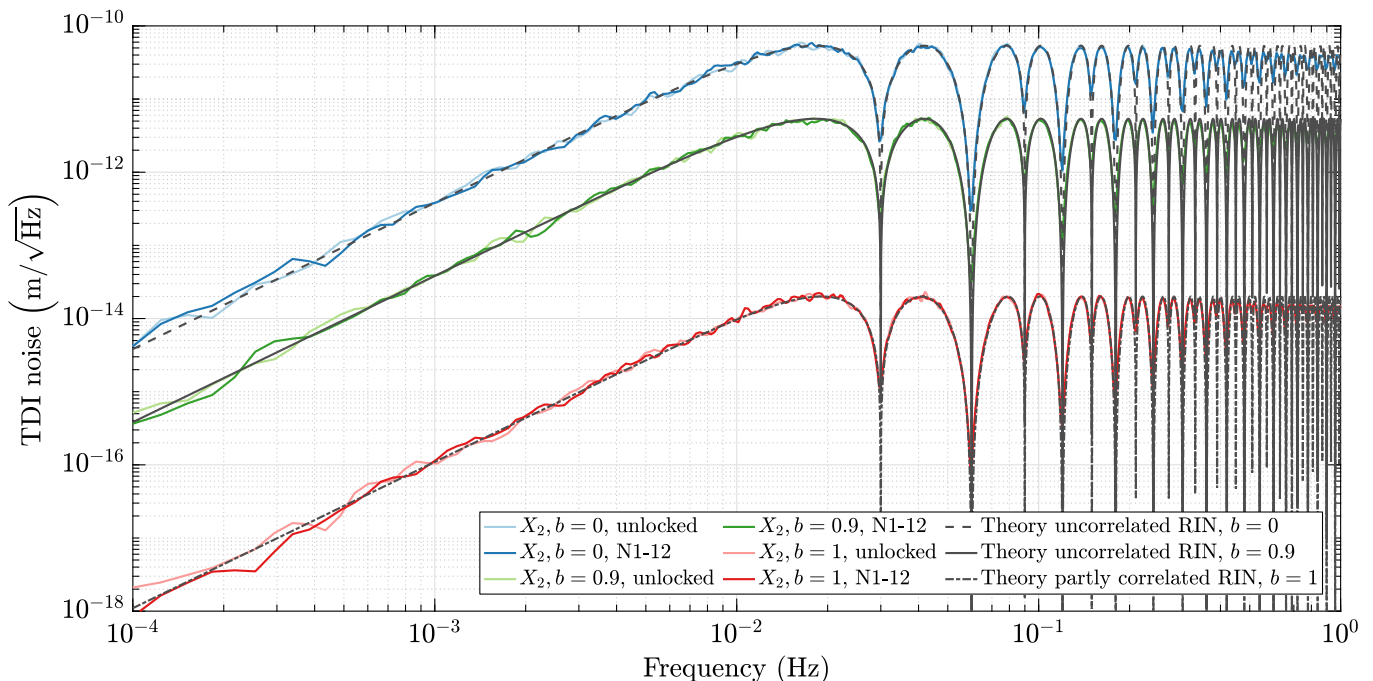


FIG. 10. Propagation of the RIN phase error through TDI, with a simulation duration of 1×10^5 s and $f_s = 1000$ Hz, for different balancing efficiencies and a comparison between unlocked lasers and the N1-12 locking scheme. We see that the RIN phase error behaves like an ISI uncorrelated readout noise. This plot has been produced with the lpsd algorithm [17]. The theoretical expectations are plotted without the usual relaxation towards lower frequencies.

Due to Doppler shifts and frequency planning, the RIN coupling can essentially be considered as an uncorrelated readout noise, and behaves as such when it is propagated through TDI.

We confirm that an additional mitigation of 1f- and 2f-RIN in the local $\text{TMI}_{ij} - \text{RFI}_{ij}$ can be achieved by choosing an interferometric operating point close to 0 rad. This, however, cannot lead to perfect cancellation due to the unequal power levels.

In the DWSs, both 1f-RIN and 2f-RIN are expected to be strongly suppressed due to the recombination of correlated neighboring quadrants with almost equal powers, and therefore good common-mode suppression characteristics.

Future work may be focused on verifying our results using actual hardware representative of the real LISA system, as well as failure studies and the more detailed analysis of the physical effects influencing the balancing efficiency.

ACKNOWLEDGMENTS

The authors would like to thank M. Misfeldt for his insightful comment.

The Albert Einstein Institute gratefully acknowledges the support of the German Space Agency, DLR. The work is supported by the Federal Ministry for Economic Affairs and Energy based on a resolution of the German Bundestag (FKZ 500Q0501, FKZ 500Q1601 and FKZ 500Q1801).

J.B.B. gratefully acknowledges support from UK Space Agency (grant ST/X002136/1). UKATC also acknowledges support from the UK Space Agency.

O.H. gratefully acknowledges support by Centre National d'Études Spatiales (CNES) and by the Programme National GRAM of CNRS/INSU with INP and IN2P3 co-funded by CNES.

[1] P. Amaro-Seoane *et al.*, Laser interferometer space antenna, arXiv preprint arXiv:1702.00786 (2017).
 [2] ISA Science Study Team, LISA Science Requirements Document ESA-L3-EST-SCI-RS-001-i1.0, (2018).
 [3] M. Armano *et al.*, Sub-Femto-g Free Fall for Space-Based Gravitational Wave Observatories: LISA Pathfinder Results, PHYSICAL REVIEW LETTERS **116**,

10.1103/PhysRevLett.116.231101 (2016).
 [4] M. Armano *et al.*, Beyond the Required LISA Free-Fall Performance: New LISA Pathfinder Results down to 20 μ Hz, PHYSICAL REVIEW LETTERS **120**, 10.1103/PhysRevLett.120.061101 (2018).
 [5] M. Armano *et al.*, Sensor noise in LISA Pathfinder: In-flight performance of the optical test mass readout, Phys.

- Rev. Lett. **126**, 131103 (2021).
- [6] M. Armano, H. Audley, J. Baird, P. Binetruy, M. Born, D. Bortoluzzi, N. Brandt, E. Castelli, A. Cavalleri, Cesarini, *et al.*, Sensor noise in lisa pathfinder: An extensive in-flight review of the angular and longitudinal interferometric measurement system, *Phys. Rev. D* **106**, 082001 (2022).
- [7] K. Abich, A. Abramovici, B. Ampanan, A. Baatzsch, B. B. Okiihiro, D. C. Barr, M. P. Bize, C. Bogan, C. Braxmaier, M. J. Burke, *et al.*, In-orbit performance of the grace follow-on laser ranging interferometer, *Phys. Rev. Lett.* **123**, 031101 (2019).
- [8] F. B. Estabrook, M. Tinto, and J. W. Armstrong, Time-delay analysis of lisa gravitational wave data: Elimination of spacecraft motion effects, *Phys. Rev. D* **62**, 042002 (2000).
- [9] D. Q. Nam, Y. Lemiere, A. Petiteau, J.-B. Bayle, O. Hartwig, J. Martino, and M. Staab, *Tdi noises transfer functions for lisa* (2022).
- [10] L. Wissel, A. Wittchen, T. S. Schwarze, M. Hewitson, G. Heinzel, and H. Halloin, Relative-intensity-noise coupling in heterodyne interferometers, *Phys. Rev. Applied* **17**, 024025 (2022).
- [11] O. Hartwig and J.-B. Bayle, Clock-jitter reduction in LISA time-delay interferometry combinations, *Phys. Rev. D* **103**, 123027 (2021), arXiv:2005.02430 [astro-ph.IM].
- [12] O. Hartwig, *Instrumental modelling and noise reduction algorithms for the Laser Interferometer Space Antenna*, Ph.D. thesis, Leibniz U., Hannover (2021).
- [13] O. Gerberding, B. Sheard, I. Bykov, J. Kullmann, J. J. E. Delgado, K. Danzmann, and G. Heinzel, Phasemeter core for intersatellite laser heterodyne interferometry: modelling, simulations and experiments, *Classical and Quantum Gravity* **30**, 235029 (2013).
- [14] G. Heinzel, M. D. Álvarez, A. Pizzella, N. Brause, and J. J. E. Delgado, Tracking length and differential-wavefront-sensing signals from quadrant photodiodes in heterodyne interferometers with digital phase-locked-loop readout, *Phys. Rev. Applied* **14**, 054013 (2020).
- [15] G. Heinzel, *LISA Frequency Planning - LISA-AEI-INST-TN-002 1.0*, Tech. Rep. (Albert Einstein Institute, 2018).
- [16] W. Adler, cornerplot, <https://github.com/wtadler/cornerplot> (2022).
- [17] M. Tröbs and G. Heinzel, Improved spectrum estimation from digitized time series on a logarithmic frequency axis, *Measurement* **39**, 120 (2006).
- [18] M. Staab, J.-B. Bayle, and O. Hartwig, *Pytdi* (2022).